Nat Hazards
DOI 10.1007/s11069-017-2919-y

ORIGINAL PAPER

Snow avalanches striking water basins: behaviour of the avalanche's centre of mass and front

G. Zitti[1] · C. Ancey[2] · M. Postacchini[1] · M. Brocchini[1,2]

Received: 4 November 2016 / Accepted: 8 May 2017

Abstract We study the behaviour of a low-density granular material entering a water basin by means of a simplified two-dimensional model, with the aim to understand the dynamics of a snow avalanche impacting a water basin like an alpine lake or a fjord. The low density of the impacting mass induces an uplift buoyancy force and, consequently, a complicated interaction between the solid and fluid phase. This paper provides an insight into the motion of the impacting mass, by presenting a simplified, two-dimensional model, where the snow is described by a low-density granular material. First, small-scale experiments, based on the Froude similarity with snow avalanches, are used to evaluate the motion of reference points of the impacting mass, i.e. the front (F), centre of mass (C) and deepest point (L). Then, applying the mass and momentum conservation principles to a fixed volume, we show that the mean motion of the impacting mass is similar to that of a damped oscillator. The stretch of the impacting mass motion is described through the motion of the reference points F and L.

Keywords Froude similarity · Impact · Small-scale experiments · Snow avalanches · Water basin

List of symbols

b	Width of the control volume
$c_{\mathrm{D}}(\boldsymbol{x}, t)$	Drag coefficient
d_{s}	Grain diameter
$\boldsymbol{D}(t)$	Dissipation tensor
$f_{\mathrm{v}}(\boldsymbol{x}, t)$	Voidage function of the drag force
$\boldsymbol{f}_{\mathrm{s}}(\boldsymbol{x}, t)$	Interaction force of the ith phase with the other phase
$\boldsymbol{f}_{\mathrm{s}}^{\mathrm{D}}(\boldsymbol{x}, t)$	Drag force on the solid phase

✉ G. Zitti
g.zitti@univpm.it

1 DICEA, Università Politecnica delle Marche, Ancona, Italy

2 ENAC/IIC/LHE, Ecole Polytechnique Fédérale de Lausanne, Lausanne, Switzerland

Published online: 18 May 2017

$Fr = \frac{u_0}{\sqrt{gh}}$	Avalanche Froude number
$\boldsymbol{g} = \begin{bmatrix} 0 \\ g \end{bmatrix}$	Gravitational field vector
h	Still water depth
$\boldsymbol{I}$	Identity tensor
$K = \frac{k}{\beta_1}$	Elastic coefficient of the motion law of the solid phase centre of mass
k	Relation between the relative vertical position of the solid phase and $1 - \frac{\rho_f}{\rho_s}\sigma(t^*)$
M	Total mass of the avalanche
$M^* = \frac{M}{\rho_f b h^2}$	Dimensionless mass
$M_s(t)$	Mass of avalanche in the control volume
$\boldsymbol{n_y} = \begin{bmatrix} 0 \\ 1 \end{bmatrix}$	Direction of the gravitational field
$\boldsymbol{r}_i(\boldsymbol{x}, t)$	Resultant of the external forces on the ith phase
$\boldsymbol{R}_s(t)$	Resultant of the external forces on the solid phase
$s(t)$	Avalanche thickness
$\bar{s}$	Mean avalanche thickness
$\bar{s}^*$	Dimensionless mean avalanche thickness
$s^*(t^*) = s(t)/h$	Dimensionless avalanche thickness
t	Time coordinate
$t^* = t\sqrt{g/h}$	Dimensionless time
$\boldsymbol{t}_s(t)$	Integral of the divergence of the solid stress tensor
$\boldsymbol{T}_i(\boldsymbol{x}, t)$	Stress tensor in the ith phase
u_0	Absolute value of the velocity of the particles at impact
$\boldsymbol{u}_0$	Mean velocity of the particles at impact
$\boldsymbol{u}_0^* = \boldsymbol{u}_0/\sqrt{gh}$	Dimensionless mean velocity of the particles at impact
$\boldsymbol{u}_i(x, t)$	Velocity of the ith phase
$\bar{\boldsymbol{u}}_i(t)$	Volume-averaged velocity of the ith phase
$\bar{\boldsymbol{u}}_s^*(t^*) = \bar{\boldsymbol{u}}_s(t)/\sqrt{gh}$	Dimensionless volume-averaged velocity of the solid phase
$\bar{u}_{sx}^*(t^*)$	Dimensionless horizontal volume-averaged velocity of the solid phase
$\bar{u}_{sy}^*(t^*)$	Dimensionless vertical volume-averaged velocity of the solid phase
v_{x0}	Initial horizontal velocity of the solid phase centre of mass
v_{y0}	Initial vertical velocity of the solid phase centre of mass
V	Control volume
$V_s(t)$	Volume of the solid phase in the control volume
x	Horizontal distance from the still water shoreline
$\boldsymbol{x}$	Vector of space coordinates
$\boldsymbol{x}_C(t)$	Position of the solid phase centre of mass
$x_C^*(t^*) = \frac{x_C}{h}$	Relative horizontal position of the solid phase centre of mass
y	Depth from the still water free surface

$y_C^*(t^*) = \frac{y_C}{h}$	Relative vertical position of the solid phase centre of mass
$\alpha_i(x,t)$	Local volume fraction of the ith phase
$\beta_{1,2}$	Average coefficients
$\varepsilon_m(i_C^*)$	Average error of the fit/predictive function for i_C^*
$\delta(t)$	Volume-averaged drag function
$\delta(\boldsymbol{x},t)$	Local drag function
$\eta(x,t)$	Water elevation
θ	Inclination of the chute
$\lambda_{1,2}^* = 0.5\left(-\bar{\varphi}_y^* \pm \sqrt{\bar{\varphi}_y^{*2} - 4K}\right)$	Coefficients of the exponential part of the solution of the vertical motion
$\pi_h = \frac{Fr\bar{s}^{*0.5}}{M^*}$	Combination coefficient for the predictive function
ρ_i	Density of the ith phase
ρ_0	Bulk density of the solid phase at impact
$\sigma(t)$	Submerged fraction of solid volume
$\sigma(\boldsymbol{x},t)$	Local fraction of the solid phase interacting with the fluid phase
ϕ_0	Solid fraction of the granular bulk at impact
$\boldsymbol{\varphi}(t)$	Dissipative tensor
$\boldsymbol{\varphi}^*(t)$	Dimensionless dissipative tensor
$\varphi_x^*(t^*)$	First component of $\boldsymbol{\varphi}^*(t)$
$\varphi_y^*(t^*)$	Last component of $\boldsymbol{\varphi}^*(t)$
$\bar{\varphi}_x^* = \frac{\varphi_x^*(t^*)}{\beta_1}$	Dissipative coefficient of the horizontal component of the motion law of the solid phase centre of mass
$\bar{\varphi}_y^* = \frac{\varphi_y^*(t^*)}{\beta_1}$	Dissipative coefficient of the vertical component of the motion of the solid phase centre of mass
$\psi(t^*) = \varphi_y^*(t^*)\dot{y}_C^*(t^*)$	Dissipation of the vertical motion

Subscript

f	Fluid phase
s	Solid phase

1 Introduction

An increasing interest on the problem of snow avalanches striking water basins has been fostered by a number of events occurred in the last two decades. Several water basins placed near dwellings were struck by snow avalanches: the lake above the village of Göschenen (Switzerland) in February 1999; a reservoir for artificial snow production in Pelvoux (France) in March 2006; the fjord of Súðavík (Iceland), where a 10-m high wave damaged several structures in October 1995; and the Lillebukt bay in the island of Stjernoya in the Altafjord (Northern Norway), impacted by avalanches sliding from the Nabbaren mountains (Frauenfelder et al. 2014).

The main concern of researchers and engineers has been the characterization of the avalanche-generated impulse waves (Fuchs et al. 2011; Naaim 2013; Zitti et al. 2016), because of its destructive potential, but there is no study on the motion of the impacted mass to the authors' knowledge. However, the description of the motion and deformation of the snow bulk after entering water is of great interest. In particular, the knowledge of the bulk geometry and its underwater motion is important for engineering purposes, e.g. to properly describe the induced hydrodynamics and the wave formation, and to better predict the wave propagation and the following flooding.

Our current understanding on snow avalanches striking water basins is based on analogy with other phenomena, mainly with landslides striking water basins. For rock avalanches and landslides, many studies have been carried out and most of them focused on the dynamics of landslide-generated impulse waves (Noda 1970; Kamphuis and Bowering 1970; Slingerland and Voight 1979; Harbitz et al. 1993; Pelinovsky and Poplavsky 1996). Many laboratory experiments have been conducted to gain insight into the physics of impulse waves and provided empirical equations for computing the impulse wave features (Huber and Hager 1997; Fritz et al. 2003a, b; Fritz and Hager 2004; Zweifel et al. 2006; Di Risio et al. 2009; Heller and Hager 2014; Romano et al. 2016). Because of their high cohesion and density, landslides are often modelled as rigid bodies that slide over a given slope, until they come to a halt (Monaghan et al. 2003; Grilli and Watts 2005; Lynett and Liu 2005; Montagna et al. 2011; Vacondio et al. 2013). Since rigid bodies are partially representative of landslides, granular materials have also been used to model them (e.g. Fritz et al. 2003a, b; Heller et al. 2008). Further, some results are available on the dynamics of landslides striking water basins. In particular, experimental studies on crater formation were carried out by Fritz et al. (2003a, b), while Fuchs and Hager (2015) studied the landslide deposition.

All these models, mimicking the landslide behaviour, are characterised by a high particle density, with the exception of some experiments (Heller and Hager 2010), and a small increase in slide volume (dilatancy up to 20%), typical of granular material after short flow distances (Fritz 2002). In fact, the density of the bulk materials used in most of these experiments closely matched that of natural landslide materials (i.e. density in the region of 1700 kg m^{-3}). The problem is that for snow avalanches, the bulk density ranges, on average, between 10 and 500 kg m^{-3}, depending on the avalanche type. It is unclear whether models calibrated for dense flows (e.g. rock avalanches) can be applied to flows involving lightweight materials (e.g. snow avalanches, pyroclastic flows). In other words, does the density influence the impact dynamics? Intuitively we can anticipate two traits that distinguish snow avalanches from dense flows. First, as snow avalanches involve a mixture of ice grains and air, possibly with a low liquid water content, the impact dynamics is controlled by the momentum exchange occurring at the particle scale (from 1 mm to 10 cm, on average, depending on the size of ice grains and snow chunks). The discrete nature of the flows is, thus, expected to be a key parameter. Second, ice density (about 950 kg m^{-3}) is lower than water density, and therefore, once immersed, ice grains (or snow chunks when snow is cohesive) experience a positively buoyant force, which causes them to rise to the free surface.

Hence, the present paper takes advantage of the discrete nature of snow flows by using the analogy between avalanches and granular flows made up of positively buoyant particles. In a recent paper (Zitti et al. 2016), we proposed a simple model based on mixture theory for estimating the momentum transfer between the granular flow and water phases (in particular, wave amplitude and energy dissipation varied with the avalanche properties), without any information about the behaviour of the avalanche, as a whole, once it has penetrated the water basin. In this work, the complex behaviour of immersed granular avalanches made up of positively buoyant particles is documented. To simplify the description of the avalanche motion, we focus on some specific reference points: (1) the motion of the centre of mass (C) provides useful information about the bulk dynamics, and

(2) the motion of the deepest (L) and frontal (F) points of the avalanche describes how the bulk stretches in the water basin.

The paper is structured as follows. Section 2 describes the experimental set-up and illustrates the complex behaviour of immersed granular avalanches through a detailed example. Section 3 analyses all the experimental results, to infer a representative function of the immersed bulk's mean motion and spreading. To do so, we apply the mass and momentum conservation principles to a fixed volume, corresponding to the impact zone, in which a granular avalanche enters, relaxing the previous hypothesis of diluted and submerged solid phase. The theoretical analysis provides the structure of the representative function that is calibrated with the available experimental data. Some conclusions close the paper.

2 Experiments

The same experimental set-up of the small-scale experiments conducted by Zitti et al. (2016) and Zitti (2016) has been used for the present study. For this reason, neither the experimental set-up nor the protocol is here described in detail; hence, the reader is referred to the references for further information. The model reproduces the two-dimensional simple problem of a diluted mass striking the water surface in a flume. This scenario is far from being three-dimensional like real-world events, but it is useful for our purpose of gaining insight in the behaviour of a low-density bulk entering a water basin (see also the comparison between 2D and 3D results obtained for landslide-tsunamis by Heller and Spinneken 2015).

To devise the experimental protocol, we use the Froude similarity between real-world and laboratory avalanches. The set-up was composed of a wooden chute, with slope angle $\theta = 30°$, whose downstream end was in contact with a 3 m-long prismatic flume filled with water. Both chute and flume were 0.11 m wide. A bulk, composed of expanded clay particles, was released from a reservoir placed at the upstream end of the chute. The bulk then slid along the smooth chute and hit the water basin, generating a water wave that propagated along the flume. The density of each particle, whose diameter was of 9 mm, was of 955 kg m^{-3}, while the bulk density ranged between 67 and 240 kg m^{-3} prior to impact. As both particle and bulk densities fall within the typical ranges for snow, we assumed that the expanded clay could mimic many of the snow properties. Three different water depths were used: $h = 0.11$, 0.14 and 0.18 m. For each value of h, two lengths of the slide path were used, i.e. 0.66 and 1.21 m, in order to vary the velocity at impact u_0. The released mass M was varied from 100 g to 700 g, by increments of 100 g. An high-speed camera, located in front of the shoreline/impact zone, acquired 256 $\times$ 785-pixel images at a rate of 1000 frames per second (fps) from the sidewall. Coloured images were converted into black-and-white images, in which the white pixels corresponded to particles and the black pixels corresponded to water or air. These images allowed us to measure the velocity u_0 and the thickness $s(t)$ of the avalanche upon impact. A summary of the experimental dataset is reported in Table 1.

Small-scale flume experiments are affected by some limitations due to: (1) scale effects and (2) the two-dimensional approximation of a three-dimensional problem. The scale factor between our experiments and real-world avalanches is approximately 100, and the typical snow chunk size is in the 7–12 cm range; hence, the particles used in our experiments did not satisfy the geometrical scaling, but using smaller particles would have

Table 1 Experimental data

Exp	M (g)	h (m)	u_0 (m s^{-1})	M^*	$\bar{s}^*$	Fr
50	101	0.14	1.590	0.047	0.094	1.356
51	200	0.14	1.521	0.093	0.118	1.298
52	300	0.14	1.507	0.139	0.132	1.286
53	400	0.14	1.484	0.186	0.148	1.266
54	500	0.14	1.434	0.232	0.167	1.224
55	601	0.14	1.438	0.279	0.152	1.227
56	700	0.14	1.442	0.325	0.171	1.230
57	100	0.14	2.182	0.046	0.082	1.862
58	200	0.14	2.052	0.093	0.108	1.751
59	299	0.14	2.025	0.138	0.107	1.728
60	402	0.14	2.033	0.186	0.112	1.735
61	498	0.14	1.914	0.231	0.133	1.633
62	600	0.14	1.854	0.278	0.145	1.582
63	685	0.14	1.806	0.318	0.127	1.541
64	98	0.18	1.551	0.028	0.038	1.167
65	198	0.18	1.496	0.055	0.042	1.126
66	300	0.18	1.424	0.084	0.059	1.072
67	400	0.18	1.469	0.112	0.056	1.105
68	497	0.18	1.394	0.139	0.064	1.049
69	597	0.18	1.240	0.168	0.081	0.933
70	689	0.18	1.112	0.193	0.069	0.837
71	101	0.18	1.942	0.028	0.026	1.461
72	199	0.18	2.024	0.056	0.041	1.523
73	300	0.18	1.930	0.084	0.045	1.453
74	401	0.18	1.801	0.112	0.055	1.355
75	484	0.18	1.945	0.136	0.053	1.464
76	599	0.18	1.818	0.168	0.063	1.368
77	696	0.18	2.012	0.195	0.072	1.514
108	101	0.11	1.975	0.076	0.081	1.901
109	200	0.11	1.867	0.150	0.119	1.797
110	297	0.11	1.916	0.223	0.121	1.845
111	396	0.11	1.841	0.298	0.112	1.772
112	500	0.11	1.841	0.376	0.178	1.772
113	600	0.11	1.943	0.450	0.107	1.871
114	701	0.11	1.696	0.526	0.162	1.633
115	101	0.11	1.587	0.076	0.085	1.527
116	192	0.11	1.623	0.144	0.126	1.562
117	300	0.11	1.524	0.226	0.132	1.467
118	400	0.11	1.528	0.300	0.129	1.471
119	495	0.11	1.373	0.372	0.169	1.321
120	588	0.11	1.412	0.442	0.211	1.359
121	702	0.11	1.242	0.527	0.306	1.196

entailed undesirable effects, related, among other aspects, to surface tension (see Zitti et al. 2016). Heller et al. (2008) showed that Froude similarity results in significant scale effects, due to surface tension and fluid viscosity, which affect the impulse wave amplitude when a reduced water depth ($h < 0.20$ m) is used for a 0.50 m wide flume. The particle dimensions in our experiments minimize surface tension effects, but the relatively small size of the flume likely entails scale effects. Hence, we are aware that the results of the experiments, especially those associated with the smaller water depths, are affected by scale effects. However, though Heller et al. (2008) stated that scale effects cause a decrease in wave amplitude when $h < 0.20$ m, we did not observe any decrease in the scaled wave amplitude spanning from the deepest to the shallowest flow experiments (for more details, the reader may refer to section 6 of Zitti et al. 2016).

Black-and-white images were also used to track the evolution of the avalanche front. Only the immersed part was analysed. First, the centre of mass C and the boundary of such immersed avalanche were determined and stored for each frame. The horizontal and vertical position $\boldsymbol{x} = \begin{bmatrix} x \\ y \end{bmatrix}$ of each stored point was defined as the horizontal distance from the shoreline and the vertical distance downward from the initial free surface, respectively (see Fig. 1). The front and bottom edges were tracked. A few particles drifted away significantly from the bulk, and so they were ignored in the boundary determination. This does not affect the calculation of the mass to any significant degree, because they are a small percentage of the particles. The frontal point of the avalanche F was defined as the farthest point from the shoreline, while the lowest edge point L was taken to be the deepest point. An image of the impacting mass is shown in Fig. 1, where the white line represents the avalanche boundary and some drifted particles are visible outside the boundary.

Figure 2 shows a typical example (experiment 68, mass of about 500 g and impact velocity of about 1.4 m s^{-1}) of the available data. The two panels illustrate the evolution in time of the horizontal (top panel) and vertical (bottom panel) coordinates of the reference points. The green, blue and red lines give the centre of mass C, the front point F and the lowest edge point L, respectively.

It has been assumed that the mean position of the immersed particles can be approximated with the position of the immersed bulk's centre of mass $\boldsymbol{x}_{\mathrm{C}} = \frac{1}{V_{\mathrm{s}}(t)} \int_{V_{\mathrm{s}}(t)} \boldsymbol{x} \mathrm{d}V$, being $V_{\mathrm{s}}(t)$ the volume of the immersed solid phase. The horizontal coordinate (green line in the

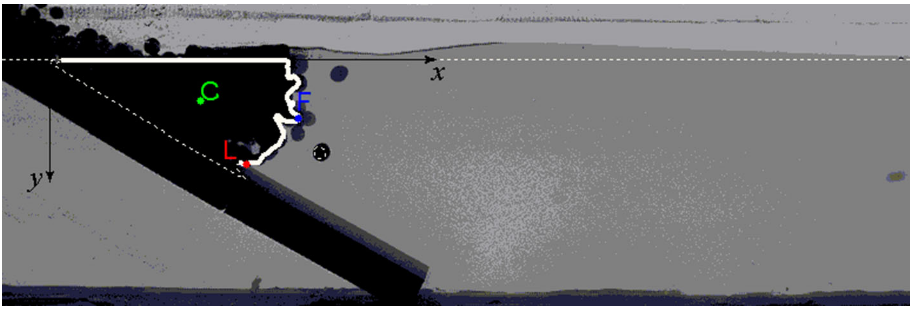

Fig. 1 Example of the image processing (experiment 68, frame 700). The *horizontal dotted line* represents the initial still water surface, the *marked line* around the mass is the portion of the boundary used to evaluate the check points, while the *dotted line* is the neglected portion (a slot of 10 mm close to the chute, where the image processing is sometimes affected by the particles' shadow on the chute, is not considered). The check points are reported: frontal point F in *blue*, the lower edge point L in *red* and the centre of mass C in *green*

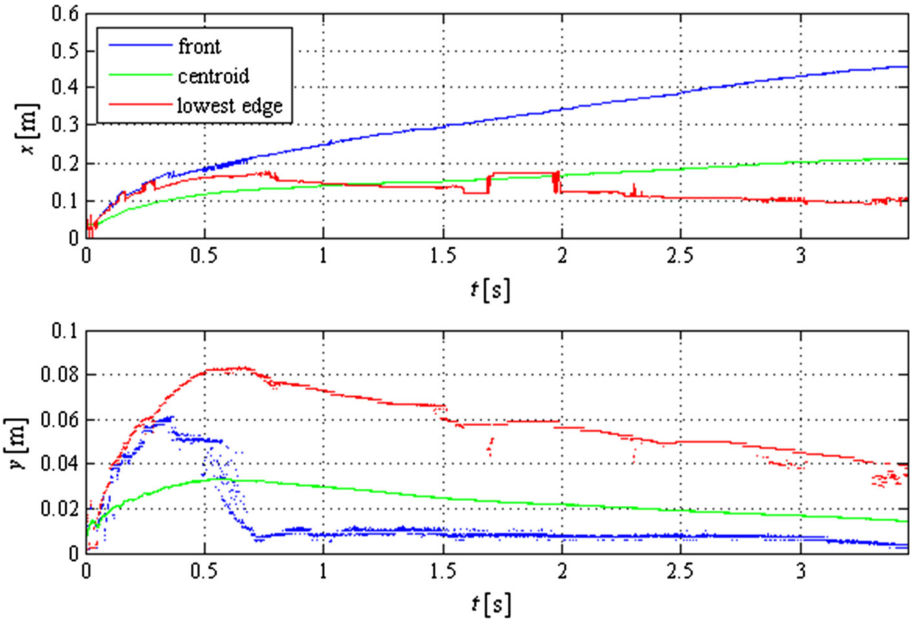

Fig. 2 Motion of the check points for experiment 68 (see Table 1 for the corresponding avalanche characteristics). Evolution of the *horizontal* and *vertical* components of the motion (initial time corresponds to the first particle entering the water), respectively, in the *top* and *bottom panel*

top panel of Fig. 2) always increased with decreasing slope, which means that the bulk moved, on average, with a decreasing velocity. By contrast, the vertical coordinate (green line in the bottom panel of Fig. 2) was typical of the water entry of lightweight particles: they first sink and, subsequently, float to the free surface.

The evolution of the frontal and deepest points had a more complicated behaviour. At short times, the horizontal position of the front F coincided with the position of the deepest point L, which means that during the initial phase of penetration, when the immersed bulk was composed of few particles only, the front was in the lowest part of the mass. When the avalanche started to spread in the water, the two points F and L were distinguishable. The horizontal coordinate of F always increased: first with decreasing slope and, eventually, with a constant slope. The horizontal coordinate of L first increased, then reached a maximum value (at $t \approx 0.75$ s) and, eventually, started decreasing, but at a small rate. With regard to the vertical motion of F and L, we noted that, initially, the vertical coordinates increased, then decreased, in agreement with physical intuition, but the front F rose significantly faster than the lowest edge point L: as the former almost immediately went back up to reach a constant value ($y \approx 0.01$ m), the latter rose slowly and continuously. The slow backward and rising motion of L can be explained by the densification that occurs in time at the rear of the avalanche, due to the incoming particles.

While the vertical motion of the centre of mass bears resemblance with a damped oscillator, the other reference points (F and L) reveal a more complicated behaviour: a fast expansion if we focus on F, and a slow stretching if we look at L.

3 The motion of the impacting mass

The motion of a dilute positively buoyant granular mixture hitting a water basin can be described through the bulk's space-averaged motion and the expansion of its boundaries. The time evolution of the centre of submerged mass is a good indicator of the average motion, while the reference points F and L can be used as proxies of the avalanche spreading in the water. The motion of the reference points for all the experiments is reported in Figs. 3, 4 and 5 (black dots). We also show the ensemble averages (calculated over the entire experimental set-up, the initial time being defined as the time at which the first particle enters the water). This generalizes what we observed for Run 68 (see Fig. 2).

3.1 The mean motion of the impacting mass

The impacting bulks' centre of mass defines a smooth curve (see Fig. 3) that can likely be captured by a simple equation. Here we take inspiration from the approximate multi-phase model proposed in Zitti et al. (2016), where the mass and momentum balance equations are applied to a fixed volume (see Fig. 6), but relaxing the hypothesis of diluted and submerged solid phase. The derivation has been shifted to Appendix 1 for the sake of brevity. We end up with the following dimensionless governing equation for the mean value of the velocity of the solid phase $\bar{\boldsymbol{u}}_{\mathrm{s}}(t)$ (Eq. 31 in "Appendix 1"):

$$\beta_1 \frac{\mathrm{d}\bar{\boldsymbol{u}}_{\mathrm{s}}^*(t^*)}{\mathrm{d}t^*} + \boldsymbol{\varphi}^*(t^*)\bar{\boldsymbol{u}}_{\mathrm{s}}^*(t^*) = \frac{s^*(t^*)}{\int_0^{t^*} s^*(\tau)\mathrm{d}\tau}\boldsymbol{u}_0^* + \left(1 - \frac{\rho_{\mathrm{f}}}{\rho_{\mathrm{s}}}\sigma(t^*)\right)\boldsymbol{n}_{\boldsymbol{y}} \tag{1}$$

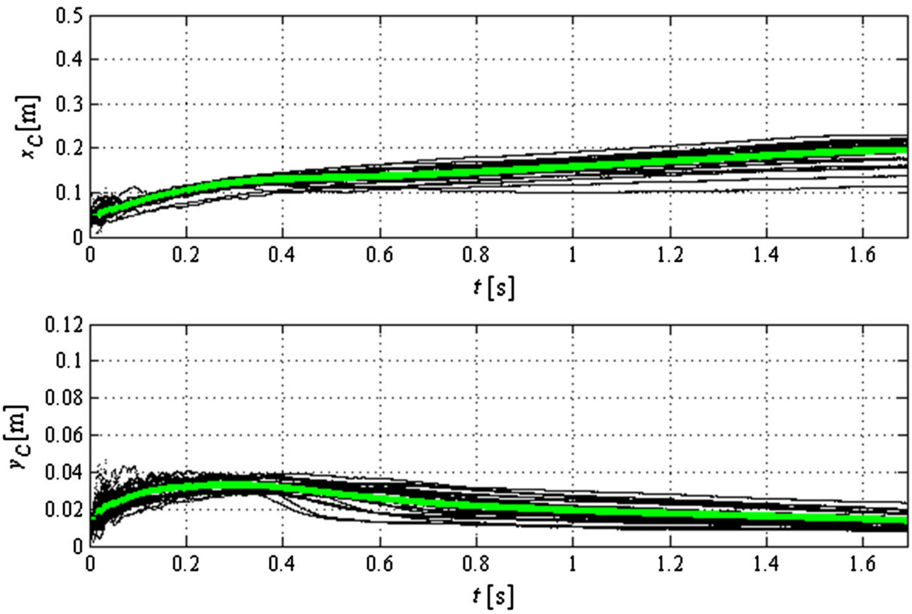

Fig. 3 Evolution in time of the centre of mass C for all the experiments (*black dots*) and ensemble averages (*green line*). The initial time corresponds to the first particle entering the water. The *horizontal* and *vertical* components are reported, respectively, in the *top panel* and in the *bottom panel*

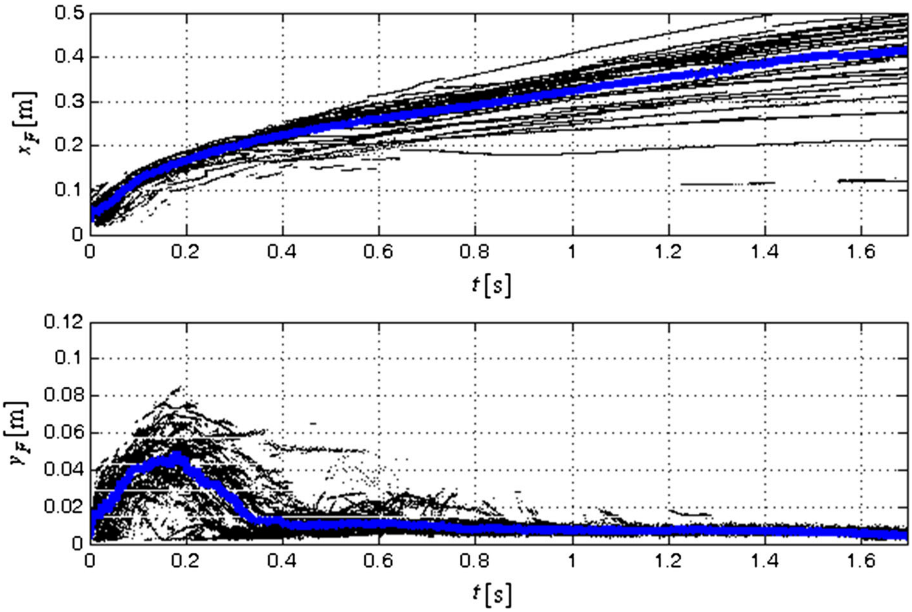

Fig. 4 Evolution in time of the front point F for all the experiments (*black dots*) and ensemble averages (*blue line*). The initial time corresponds to the first particle entering the water. The *horizontal* and *vertical* components are reported, respectively, in the *top panel* and in the *bottom panel*

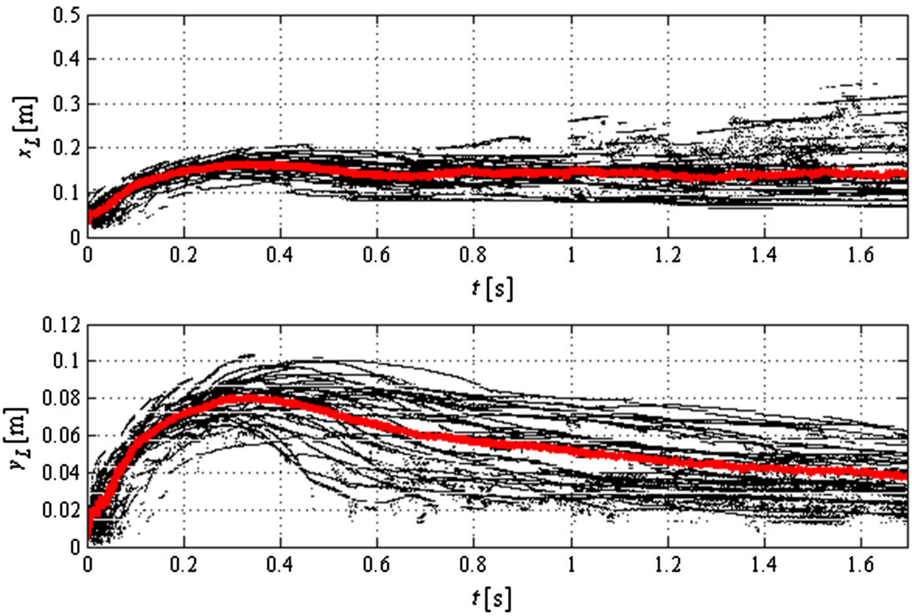

Fig. 5 Evolution in time of the lowest edge point L for all the experiments (*black dots*) and ensemble averages (*red line*). The initial time corresponds to the first particle entering the water. The *horizontal* and *vertical* components are reported, respectively, in the *top panel* and in the *bottom panel*

Fig. 6 Schematic of the control volume

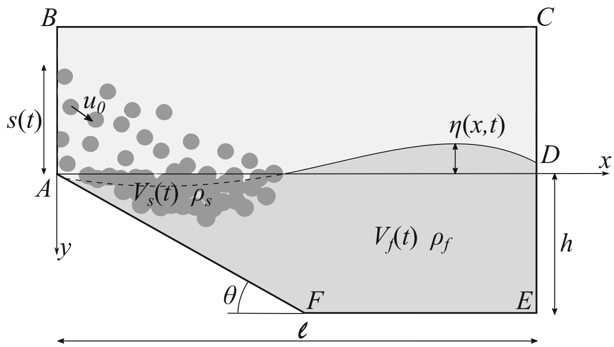

where $\bar{\boldsymbol{u}}_{\mathrm{s}}^{*}$ is the dimensionless mean velocity of the solid phase, t^{*} is the dimensionless time, β_1 is an average coefficient of the solid phase momentum (i.e. the ratio of the mean momentum to the product of the mean mass and mean velocity of the solid phase), $\boldsymbol{\varphi}^{*}(t^{*})$ is the dimensionless dissipation function, $s^{*}(t^{*})$ is the relative avalanche thickness, $\boldsymbol{u}_0^{*}$ is the relative mean velocity of the solid phase upon impact, ρ_{f} is the fluid density, ρ_{s} is the solid density, $\sigma(t^{*})$ is the dimensionless fraction of the submerged mass, and the unit vector $\boldsymbol{n}_{\boldsymbol{y}}$ points in the vertical direction (for a clearer description, the reader is referred to "Appendix 1"). Equation (1) is a differential equation of the mean velocity of the solid phase and is representative of the motion of the centre of mass of the impacting bulk, i.e. $\dot{\boldsymbol{x}}_{\mathrm{C}}^{*}(t^{*}) = \frac{1}{h}\dot{\boldsymbol{x}}_{\mathrm{C}}(t^{*}) \sim \bar{\boldsymbol{u}}_{s}^{*}(t^{*})$, where the over-dot means time derivation. The equation is rather simple and fairly similar to the equation of a forced harmonic oscillator with time-depending coefficients. The number of time-depending coefficients prevents us from finding a close solution without further assumptions. Instead of searching for a close solution, we are going to derive a representative function for the mean motion of the solid phase by taking advantage of the similitude of Eq. (1) with the harmonic oscillator. Since the general solution of the differential equation of an harmonic oscillator provides the shape of the solution, we neglect the inhomogeneous part, i.e. the first term on the right-hand side of Eq. (1), which represents the external force for the differential equation. The last term on the right-hand side is included in the homogenous part of the differential equation, as the submerged mass fraction $\sigma(t^{*})$ implicitly depends on the mean position of the submerged mass. Hence, we find that the x and y projections of Eq. (1) are:

$$\beta_1 \ddot{x}_C^{*}(t^{*}) + \varphi_x^{*}(t^{*})\dot{x}_C^{*}(t^{*}) = 0 \tag{2a}$$

$$\beta_1 \ddot{y}_{\mathrm{C}}^{*}(t^{*}) + \varphi_y^{*}(t^{*})\dot{y}_{\mathrm{C}}^{*}(t^{*}) = \left(1 - \frac{\rho_{\mathrm{f}}}{\rho_{\mathrm{s}}}\sigma(t^{*})\right) \tag{2b}$$

where $\varphi_x^{*}(t^{*})$ and $\varphi_y^{*}(t^{*})$ are the two components of the diagonal dissipation tensor $\boldsymbol{\varphi}^{*}(t)$. The two projected equations are then studied separately.

From Eq. (2a) we get the following relation between mean acceleration and mean velocity:

$$\ddot{x}_{\mathrm{C}}^{*}(t^{*}) = -\frac{\varphi_x^{*}(t^{*})}{\beta_1}\dot{x}_{\mathrm{C}}^{*}(t^{*}) \tag{3}$$

Since $\frac{\varphi_x^{*}(t^{*})}{\beta_1}$ is always positive, Eq. (3) states that the horizontal acceleration is always opposite to the horizontal velocity. Therefore, the initial velocity being positive, the initial

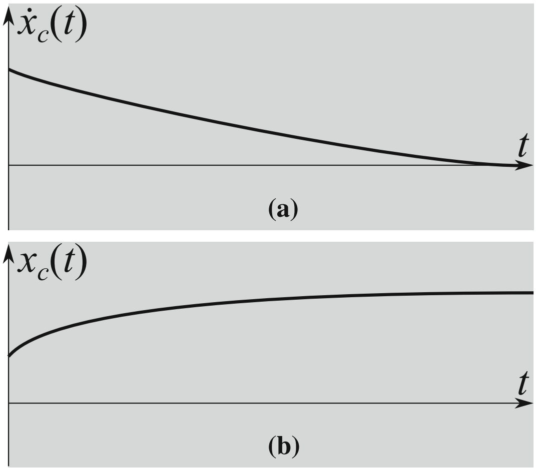

Fig. 7 Representation of the horizontal velocity (**a**) and horizontal position (**b**) of the solid phase centre of mass $x_C(t)$

acceleration is negative, thus causing the velocity to vanish (see Fig. 7a). Consequently, the horizontal displacement of the immersed bulk's centre of mass increases, but with a decreasing rate, until it reaches steady state. The representation of such motion, shown in Fig. 7b, is very similar to the solution of a simply damped motion.

Equation (2b) is more complicated to analyse, since it includes the submerged mass fraction $\sigma(t^*)$, which implicitly depends on the mean position of the submerged mass. To handle such complication, we rearrange Eq. (2b) to get $\sigma(t^*)$:

$$\sigma(t^*) = \frac{\rho_s}{\rho_f}\left(1 - \beta_1 \ddot{y}^*_C(t^*) - \psi(t^*)\right) \tag{4}$$

where $\psi(t^*) = \varphi^*_y(t^*)\dot{y}^*_C(t^*)$ is the dimensionless dissipation occurring during the motion. Taking advantage of a graphical representation of the motion in the $(\sigma(t^*), \psi(t^*))$-plane, illustrated in Fig. 8a, we deduce the behaviour of the vertical flow component. Since this analysis requires a careful use of the plane, an explanation of how the plane should be read is detailed in Appendix 2. Analysing the motion in the $(\sigma(t^*), \psi(t^*))$-plane allows us to define the function that describes the mean vertical position of the avalanche, reported in Fig. 8b. Note the similarities with the solution of a simply damped harmonic oscillator.

The motion shown in Figs. 7b and 8b is similar to our experimental data (Fig. 3a, b). Furthermore, it is also similar to the solutions of simple ordinary differential equations. In particular, the horizontal motion is similar to the solution of a simple damping, while the vertical motion is similar to the solution of a simply damped harmonic oscillator. This suggests reducing Eq. (2) to simpler differential equations and using their solutions to describe the mean motion of the impacting solid phase. Simplifying Eq. (2), described in the following, involves several assumptions.

Equation (2) can be reduced to simpler ordinary differential equations if all the coefficients not involving the motion itself (i.e. $\varphi^*_x(t^*)$ and $\varphi^*_y(t^*)$) are assumed to be constant. This means that the rate of change in the energy dissipation term (see Eq. 29) is of minor importance to the motion. In addition, the vertical component can become that of a simply

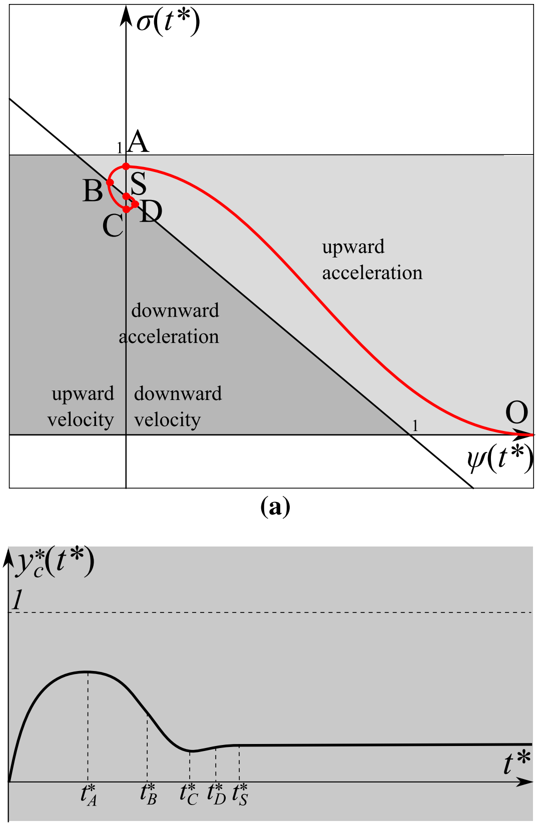

(b)

Fig. 8 **a** $(\sigma(t^*), \psi(t^*))$-plane used to represent the evolution of the motion. The condition of zero velocity corresponds to the ordinate $\dot{y}^*_{\mathrm{C}}(t^*) = 0$. The inclined *straight line* gives the zero acceleration condition $\ddot{y}^*_{\mathrm{C}}(t^*) = 0$. The *red curve* represents the motion path in the case of a low-density material, such as a snow avalanche. **b** Representation of the centre of mass vertical motion $y^*_{\mathrm{C}}(t^*)$ of the solid phase for the case of snow avalanches impacting water, characterized by one evident oscillation

damped harmonic oscillator if the term depending on the fraction of the submerged mass is taken to be linearly dependent on the average position of the centre of mass:

$$\left(1 - \frac{\rho_{\mathrm{f}}}{\rho_{\mathrm{s}}}\sigma(t^*)\right) \propto k y^*_{\mathrm{C}}(t^*) \tag{5}$$

Equation (5) provides a relation between the percentage of the submerged body and the depth of its centre of mass.

Using the assumptions above, we obtain the following solvable ordinary differential equations:

$$\begin{cases} \ddot{x}^*_{\mathrm{C}}(t^*) + \bar{\varphi}^*_x \dot{x}^*_{\mathrm{C}}(t^*) = 0 \\ \ddot{y}^*_{\mathrm{C}}(t^*) + \bar{\varphi}^*_y \dot{y}^*_{\mathrm{C}}(t^*) + K y^*_{\mathrm{C}}(t^*) = 0 \end{cases} \tag{6}$$

where $\bar{\varphi}^*_x = \frac{\varphi^*_x(t^*)}{\beta_1}$, $\bar{\varphi}^*_y = \frac{\varphi^*_y(t^*)}{\beta_1}$ and $K = \frac{k}{\beta_1}$ are constant coefficients. General solutions of system (6) are:

$$
\begin{cases}
x_{\mathrm{C}}^{*}(t^{*}) = x_{\mathrm{C}}^{*}(0) + \dfrac{\dot{x}_{\mathrm{C}}^{*}(0)}{-\bar{\varphi}_{x}^{*}}\left(e^{-\bar{\varphi}_{x}^{*}t^{*}} - 1\right) \\
y_{\mathrm{C}}^{*}(t^{*}) = y_{\mathrm{C}}^{*}(0) + \dfrac{\dot{y}_{\mathrm{C}}^{*}(0)}{\lambda_{1} - \lambda_{2}}\left(e^{\lambda_{1}^{*}t^{*}} - e^{\lambda_{2}^{*}t^{*}}\right)
\end{cases} \tag{7}
$$

where $\lambda_{1,2}^{*} = 0.5\left(-\bar{\varphi}_{y}^{*} \pm \sqrt{\bar{\varphi}_{y}^{*2} - 4K}\right)$. Solutions (7) provide a simple description for the mean motion of the solid phase and, being very suitable in regressions of the experimental data, allow for the construction of suitable predictive relations for the mean motion of the solid phase.

Since expressions (7) are general solutions to Eq. (6), specific solutions are found once suitable initial conditions to Eq. (6) are provided. We, thus, assume that the initial horizontal position of the centre of mass is equal to the horizontal projection of the centre of the front of an equivalent avalanche with constant thickness $\bar{s}$ (the average avalanche thickness) at the time it reaches the water. Since the inclination of the chute is $\theta = 30°$, the initial conditions for the horizontal motion are:

$$
\begin{cases}
x_{\mathrm{C}}^{*}(0) = \dfrac{\bar{s}}{h} \\
\dot{x}_{\mathrm{C}}^{*}(0) = v_{x0}
\end{cases} \tag{8}
$$

The initial conditions for the vertical motion are:

$$
\begin{cases}
y_{\mathrm{C}}^{*}(0) = 0 \\
\dot{y}_{\mathrm{C}}^{*}(0) = v_{y0}
\end{cases} \tag{9}
$$

Substituting conditions (8) and (9) into Eq. (7), we obtain:

$$
\begin{cases}
x_{\mathrm{C}}^{*}(t) = \dfrac{v_{x0}}{-\bar{\varphi}_{x}^{*}}\left(e^{-\bar{\varphi}_{x}^{*}t^{*}} - 1\right) + \bar{s}^{*} \\
y_{\mathrm{C}}^{*}(t) = \dfrac{v_{y0}}{\lambda_{1}^{*} - \lambda_{2}^{*}}\left(e^{\lambda_{1}^{*}t} - e^{\lambda_{2}^{*}t}\right)
\end{cases} \tag{10}
$$

where $\bar{s}^{*} = \frac{\bar{s}}{h}$. Then, solutions (10) are worked out using a nonlinear least squares (NLS) regression scheme, which solves nonlinear data-fitting problems in the least-squares sense and finds the coefficients v_{x0}, v_{y0},$\bar{\varphi}_{x}^{*}$, λ_{1}^{*} and λ_{2}^{*} that provide the best fit for solutions (10) to the experimental data. An example of the fit obtained with these solutions is illustrated by the green lines in Fig. 9. Table 2 summarizes the best-fit coefficients and the average errors, evaluated as:

$$
\varepsilon_{m}\left(i_{\mathrm{C}}^{*}\right) = \frac{\left|i_{\mathrm{C}}^{*} - i_{\mathrm{C,fit}}^{*}\right|}{i_{\mathrm{C}}^{*}} \quad \text{with } i = x, y \tag{11}
$$

where $i_{\mathrm{C,fit}}^{*}$ is the fit function whose coefficients are evaluated with the regression. The average errors of the horizontal component are between 4 and 13%, while the average errors of the vertical component are between 2 and 25%. Though some significant fluctuations are displayed in Fig. 3, solutions (10) with best-fit coefficient can represent 75% of the experimental data with an error lower than 10%. Therefore, the reliability of the approximating functions (10) is confirmed.

Since solutions (10) give a good representation of the experimental data, they are used to derive predictive relations. Using, again, NLS regression, the coefficients of functions (10) are related to the avalanche characteristics that have been found to be of paramount

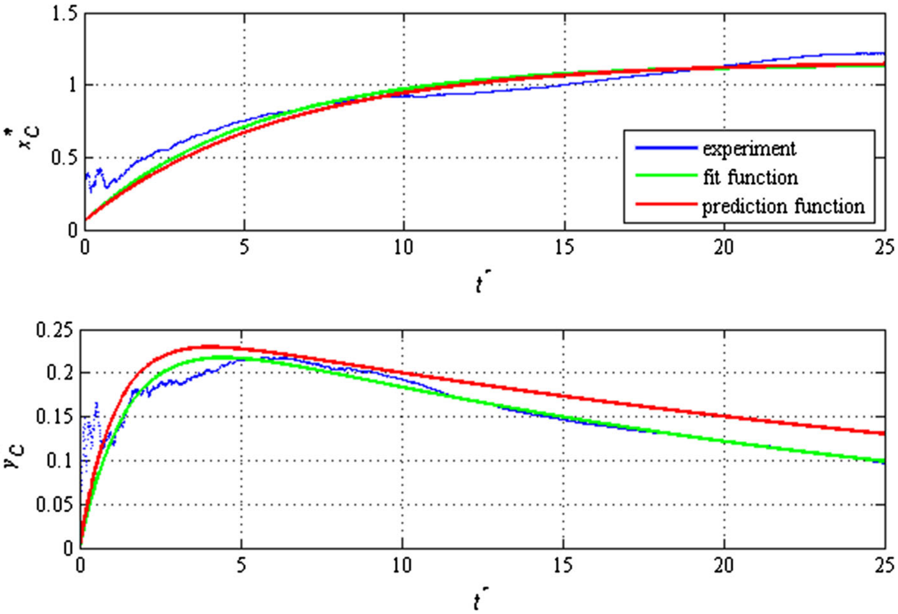

Fig. 9 Comparison of the motion of the solid phase (*blue line*) for a specific, representative, experiment ($M = 599$ g, $h = 0.18$ m and $u_0 = 1.81$ m s^{-1}) with the fit obtained using Eq. (10) (*green line*) and with the predictive relations (13) (*red line*) obtained from the avalanche fundamental parameters. The *top panel* reports the horizontal motion (fit average error 9% and prediction average error 10%), while the *bottom panel* reports the vertical motion (fit average error 5% and prediction average error 19%)

importance by Zitti et al. (2016). These are: the avalanche dimensionless mass $M^* = \frac{M}{\rho_f b h^2}$, the avalanche dimensionless thickness $\bar{s}^*$ and the avalanche Froude number $Fr = \frac{u_0}{\sqrt{gh}}$. The regression gives the following relations for the above-mentioned coefficients:

$$\begin{aligned} \bar{\varphi}^*_x &= 0.1\pi_h^{0.7} \\ v_{x0} &= 0.12M^{*0.1}Fr^{0.3}\pi_h^{0.7} \\ \lambda^*_1 &= -0.02\pi_h^{0.5} \\ \lambda^*_2 &= -\pi_h^{0.8}M^{*0.4} \\ v_{y0} &= 0.14Fr^{1.5} \end{aligned} \tag{12}$$

with $\pi_h = \frac{Fr\bar{s}^{*0.5}}{M^*}$. Substituting relations (12) into solutions (10) gives the predictive relations for the time evolution of the centre of mass of the solid phase:

$$\begin{cases} x^*_C(t) = 1.2M^{*0.1}Fr^{0.3}\left(1 - e^{-0.1\pi_h^{0.7}t^*}\right) + \bar{s}^* \\ y^*_C(t) = \dfrac{0.14Fr^{1.5}}{\pi_h^{0.8}M^{*0.4} - 0.02\pi_h^{0.5}}\left(e^{-0.02\pi_h^{0.5}t} - e^{-\pi_h^{0.8}M^{*0.4}t}\right) \end{cases} \tag{13}$$

An example of the good description provided by these solutions is illustrated by the red lines in Fig. 9. The average error, evaluated using Eq. (11), slightly increases, ranging between 9 and 35% for the horizontal motion, and between 5 and 48% for the vertical motion (see Table 3). However, Eq. (13) properly describes the horizontal motion, with an

Table 2 Coefficients of fit functions for the horizontal and vertical motion, obtained with the NLS regression

Exp	$x_C^*(t)$			$y_C^*(t)$			
	v_{x0}	$\bar{\varphi}_x^*$	$\varepsilon_m(x_C^*)$ (%)	$A = \frac{v_{y0}}{\lambda_1^* - \lambda_2^*}$	λ_1^*	λ_2^*	$\varepsilon_m(y_C^*)$ (%)
50	0.349	0.470	8	0.214	−0.052	−2.210	16
51	0.226	0.265	10	0.236	−0.046	−1.108	11
52	0.183	0.171	11	0.258	−0.044	−0.883	7
53	0.165	0.152	10	0.231	−0.029	−1.516	3
54	0.174	0.157	11	0.256	−0.030	−0.832	3
55	0.177	0.156	9	0.255	−0.023	−0.848	4
56	0.173	0.138	9	0.260	−0.021	−0.714	5
57	0.511	0.564	10	0.333	−0.089	−2.362	25
58	0.285	0.288	11	0.307	−0.064	−1.497	16
59	0.196	0.169	13	0.296	−0.053	−1.448	11
60	0.224	0.187	10	0.297	−0.042	−1.038	6
61	0.198	0.159	10	0.278	−0.034	−1.336	5
62	0.201	0.159	9	0.274	−0.026	−1.476	5
63	0.212	0.165	10	0.316	−0.028	−0.780	3
64	0.306	0.478	9	0.172	−0.066	−2.031	20
65	0.178	0.217	13	0.189	−0.056	−1.143	12
66	0.163	0.174	11	0.218	−0.052	−0.833	7
67	0.151	0.152	10	0.223	−0.042	−0.637	5
68	0.178	0.179	10	0.219	−0.039	−0.807	3
69	0.199	0.215	9	0.233	−0.033	−0.799	3
70	0.173	0.173	10	0.212	−0.027	−0.696	3
71	0.171	0.158	12	0.247	−0.089	−3.345	18
72	0.284	0.334	10	0.268	−0.068	−1.258	13
73	0.189	0.194	13	0.228	−0.057	−1.512	11
74	0.202	0.201	11	0.266	−0.053	−0.977	7
75	0.183	0.167	11	0.255	−0.047	−0.992	5
76	0.199	0.184	9	0.279	−0.041	−0.665	5
77	0.199	0.175	9	0.250	−0.036	−0.957	4
108	0.903	0.981	7	0.530	−0.126	−0.859	13
109	0.641	0.584	8	0.405	−0.081	−1.003	9
110	0.416	0.335	8	0.368	−0.056	−1.614	7
111	0.348	0.289	8	0.344	−0.036	−1.740	5
112	0.359	0.280	7	0.343	−0.032	−1.409	4
113	0.284	0.163	11	0.326	−0.027	−1.320	4
114	0.262	0.168	10	0.331	−0.025	−1.413	2
115	0.534	0.607	6	0.533	−0.128	−0.625	8
116	0.378	0.390	4	0.361	−0.073	−0.628	8
117	0.307	0.249	9	0.264	−0.032	−1.900	5
118	0.311	0.257	9	0.282	−0.028	−1.885	3
119	0.308	0.255	6	0.293	−0.027	−1.057	4
120	0.240	0.186	5	0.319	−0.026	−0.685	5

Table 2 continued

Exp	$x^*_C(t)$			$y^*_C(t)$			
	v_{x0}	$\bar{\varphi}^*_x$	$\varepsilon_m(x^*_C)$ (%)	$A = \frac{v_{y0}}{\lambda^*_1 - \lambda^*_2}$	λ^*_1	λ^*_2	$\varepsilon_m(y^*_C)$ (%)
121	0.190	0.139	6	0.302	−0.021	−1.060	4

average error of 16%, and the vertical motion, with an average error of 21%. Further, the governing parameters for the impulse wave evolution proposed in Zitti et al. (2016) are suitable to describe also the motion of the impacting mass.

3.2 The overall motion of the impacting mass

In this section the motion of the frontal point F and of the lower edge point L of the impacting solid phase is analysed, in order to gain some insight in the overall motion of the avalanche. Inspection of experiment 68 (see Sect. 2) has revealed that, after an initial transient phase, the frontal point F advances more than the centre of mass C, while the lower edge point L moves backwards and upwards, mainly following the sloping bottom. This behaviour has been observed in most of the experiments (compare Figs. 4, 5 with Fig. 3), but in many cases isolated particles lead to steps in the signal, making it impossible to perform a systematic and efficient analysis of each experiment, as done for the centre of mass motion. However, the observation of the difference of the motion of the frontal point (F) and lower edge point (L) motion of each experiment from that of the centre of mass, illustrated in Fig. 10, respectively, in blue and red give useful insight in the inner motion of the solid phase. In fact, all the experiments show the same behaviour; hence, we believe that studying the mean difference from the motion of C can give useful insights.

The difference between the ensemble average (over all experiments) of the position of F from the ensemble average of the position of the centre of mass is characterised by a horizontal component monotonically increasing in time (average of the blue cloud in Fig. 10a). On the other hand, the vertical component initially increases, then decreases to, finally, increase again to reach a constant value (average of the blue cloud in Fig. 10b). This means that four main stages can be recognized, such that the front:

(1) advances and sinks faster than the centre of mass of the solid phase;
(2) keeps advancing, but climbs up with reference to the centre of mass;
(3) keeps advancing and sinks again;
(4) keeps advancing but reaching a constant depth.

We can deduce that the frontal area of the avalanche expands in the horizontal direction. It is also of particular interest that the damped oscillation observed for the vertical motion of the centre of mass of the solid phase corresponds to a damped oscillation for the motion of the frontal area.

The difference of the ensemble average of the position of L from the ensemble average of the centre of mass is such that both horizontal and vertical components initially increase and later slowly decrease. Two main stages are thus found for which the lower edge point:

(1) sinks and advances more than the centre of mass of the solid phase;
(2) climbs up backwards in comparison with the centre of mass of the solid phase.

Table 3 Average errors obtained using the predictive functions (13)

Exp	$\varepsilon_m\left(x_C^*\right)$ (%)	$\varepsilon_m\left(y_C^*\right)$ (%)
50	26	48
51	21	35
52	11	27
53	11	26
54	10	27
55	9	23
56	10	24
57	19	35
58	17	22
59	15	12
60	10	6
61	9	9
62	9	12
63	12	10
64	35	20
65	19	19
66	12	11
67	11	14
68	11	12
69	12	14
70	20	7
71	18	25
72	20	15
73	16	36
74	12	20
75	12	36
76	10	19
77	11	29
108	16	25
109	13	21
110	16	16
111	19	9
112	20	16
113	33	28
114	29	5
115	13	32
116	10	20
117	18	14
118	24	9
119	26	18
120	17	22
121	16	36

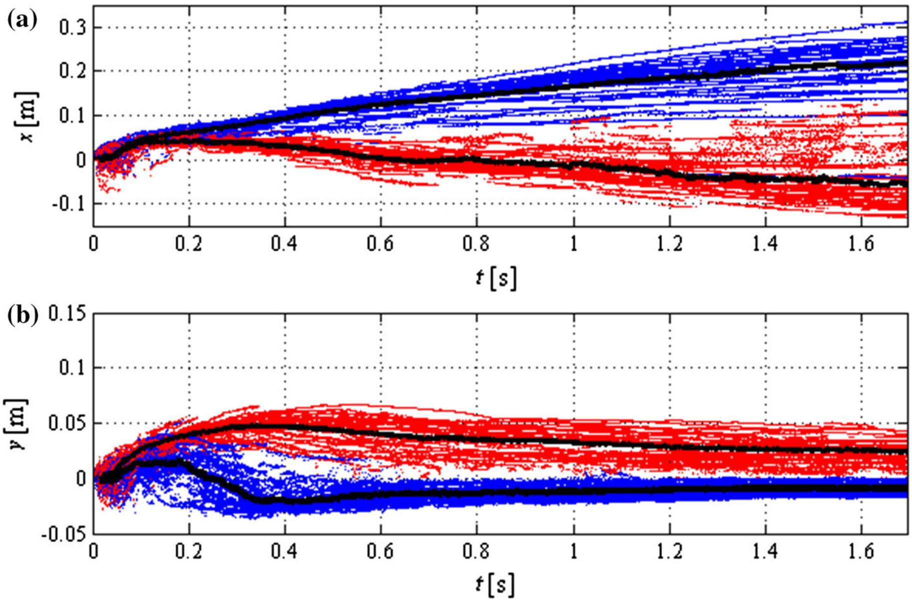

Fig. 10 Horizontal (*top panel*) and vertical (*bottom panel*) components of the deviation of the frontal point motion (*blue dots*) and of the lower edge point motion (*red dots*) from the average motion for all the experiments reported in the paper. The *black lines* in the middle of the cloud of points are the mean values over all realizations

The second stage of the motion of the lower edge, being upwards and backwards, often occurs along the chute. Furthermore, since the separation between the two stages might not be the same for the horizontal and vertical components, an intermediate phase may occur.

Combining the four phases for the frontal motion and of the two phases for the lower edge motion gives a number of possible configurations. Of particular interest is the initial phase, where both the frontal area and the lower edge area sink forward in comparison with the centre of mass. This occurs when the solid bulk expands downward, mainly in the direction of the chute inclination. Another configuration of interest, that often follows the previous one, is characterized by the front climbing up forwards and the lower edge climbing up backwards with reference to the centre of mass. This configuration is characteristic of a buoyant solid phase and highlights how floatation relates with a significant horizontal expansion of the solid bulk. Most of the expansion occurs at the front of the avalanche. In fact the backward motion of L is smaller than the forward motion of F. This is easily explained by the densification in the back of the avalanche due to incoming particles.

4 Conclusions

The dynamics of snow avalanches entering a water basin has been studied by conducting laboratory experiments satisfying the Froude similarity. The study includes both an experimental investigation, with the analysis of the motion of three significant reference points of the solid phase—i.e. the front (F), the centre of mass (C) and the lowest edge (L)—and a theoretical analysis, based on the application of the conservation principle to a fixed volume located at the flume inlet.

Representative functions of the mean motion of the solid phase have been deduced from both the experimental observations and a theoretical analysis. The latter focused on the overall dynamics of the problem. In particular, by simplifying the governing equations to ordinary differential equations (by assuming constant energy dissipation), we implicitly assumed that the actual evolution of energy dissipation is of minor importance. The dissipation function includes three terms (see Eqs. 29, 27): the inter-particle stress $\boldsymbol{t}_{\mathrm{s}}(t)$, the particle–fluid drag $\beta_2\sigma(t)V_{\mathrm{s}}(t)\delta(t)(\bar{\boldsymbol{u}}_{\mathrm{f}}(t)-\bar{\boldsymbol{u}}_{\mathrm{s}}(t))$ and a term related to the rate of change of the impacting volume ($\beta_1\rho_{\mathrm{s}}\frac{\mathrm{d}V_{\mathrm{s}}(t)}{\mathrm{d}t}$). The former two are well-known dissipative terms, while the latter represents the momentum contribution of the solid phase entering the control volume. The assumption of constant energy dissipation means that the three terms composing the dissipation balance each other, their sum being approximately constant. This suggests a simple relation between the incoming momentum of the avalanche and the particle fluid drag, which is the mechanism for the momentum transfer to the fluid phase at the particle scale (see Zitti et al. 2016). Since in our model the inter-particle dissipation is not separated from particle–fluid interaction, we cannot warrant a linear relation between the incoming momentum of the avalanche and the momentum imparted to the fluid. However, the simple relation between the incoming momentum and the two contributions justifies the simplicity of some empirical predictive relations for the generated waves available in the literature (Heller and Hager 2010; Heller and Spinneken 2015; Zitti et al. 2016), some of which are successfully applied to the real case of a tsunami caused by glacier calving (Lüthi and Vieli 2016).

The comparison of theoretical and experimental results has led to an accurate characterization of the mean motion of the impacting mass and some important insights into the overall dynamics of the solid phase. In particular, we found relations that can predict, given the sliding phase characteristics, the average motion of the avalanche with a mean error of 16% for the horizontal component and 21% for the vertical component. Such errors are consistent with the scale effects estimated by Heller and Hager (2010) for the wave amplitude when water depth is as low as $h = 0.15$ m.

Moreover, the study of the avalanche front and lower edge's motion shows that the motion of a buoyant material striking water is characterized not only by the vertical rebound due to the lower particle density, but also by a number of different processes, among which a significant horizontal expansion of the bulk volume of the solid phase. We can speculate that these processes produce local distortions inside the bulk, and consequently interactions between particles, which are larger than in landslides. These processes are significantly dissipative, hence can partly explain the low conversion factor between the avalanche energy and the wave energy found in Zitti et al. (2016).

Finally, this work is one of the first experimental studies of the dynamics of a buoyant phase entering a water body and provides data that can be used for model-validation purposes. In particular, the insights provided by this paper allow us to assess whether the numerical models, developed for landslide-generated impulse waves, can also be used for snow-avalanche-generated waves. In particular, numerical models based on the motion of rigid bodies (Grilli and Watts 2005; Lynett and Liu 2005) are not adequate since they cannot reproduce the stretching and spreading of snow into water, while two-phase numerical models (e.g. Cremonesi et al. 2010; Pudasaini and Miller 2012) are better candidates for simulating snow avalanches striking water basins. Further, the avalanche motion after striking a water basin, such as alpine lakes or fjords, provides important information for engineering purposes.

Acknowledgements The present work was started while Maurizio Brocchini was visiting the Laboratoire d'Hydraulique Environnementale, École Polytechnique Fédérale de Lausanne (EPFL). Christophe Ancey acknowledges support from the EPFL civil engineering department and from the Swiss National Science Foundation (Grant No. 200021 146271/1, a project called "Physics of Basal Entrainment").

Appendix 1: Theoretical description of the mean motion of the impacting mass

We search for a simple equation for the mean motion of the solid phase by relaxing the hypothesis of diluted and submerged solid phase used in the theoretical model proposed by Zitti et al. (2016). After defining the local problem using the set of equations of a multi-phase mixture theory, they are integrated over a two-dimensional control volume representative of the problem. The integration leads to a differential equation in terms of mean value of the velocity of the impacting particles, which is hereafter referred to as the mean motion of the impacting mass.

First, conservation principles are formulated using the theory of multi-phase mixtures (Truesdell 1984; Meruane et al. 2010), i.e. assuming that each point is occupied by a volume fraction $\alpha_i(\boldsymbol{x}, t)$ of each ith phase. Three phases are present in the problem at hand: the air, the fluid water (subscript f) and the solid phase (subscript s) composed of particles with solid density slightly lower than the fluid density. Since the air density is negligible if compared to those of water and snow, the role of the air phase can be neglected in the conservation equations (see also Zitti et al. 2016). Assuming that both the fluid and the granular material are incompressible, the balance equations for the mass and momentum of each phase are ($i = f,s$):

$$\frac{\partial \alpha_i(\boldsymbol{x}, t)}{\partial t} + \nabla \cdot (\alpha_i(\boldsymbol{x}, t)\boldsymbol{u}_i(\boldsymbol{x}, t)) = 0 \tag{14}$$

$$\rho_i\left(\frac{\partial(\alpha_i(\boldsymbol{x}, t)\boldsymbol{u}_i(\boldsymbol{x}, t))}{\partial t} + \nabla \cdot \left(\alpha_i(\boldsymbol{x}, t)\boldsymbol{u}_i(\boldsymbol{x}, t)\boldsymbol{u}_i^T(\boldsymbol{x}, t)\right)\right) = \boldsymbol{r}_i(\boldsymbol{x}, t) \tag{15}$$

where ρ_i is the density of the ith phase, while $\boldsymbol{u}_i(\boldsymbol{x}, t)$ and $\boldsymbol{r}_i(\boldsymbol{x}, t)$ are, respectively, the velocity and the resultant of the external forces referring to the ith phase, at position $\boldsymbol{x}$ and time t. Focusing on the solid phase, the resultant force is given by the divergence of the stress tensor, the gravitational body force and the interaction force with the fluid phase $\boldsymbol{f}(\boldsymbol{x}, t)$:

$$\boldsymbol{r}_\mathrm{s}(\boldsymbol{x}, t) = \nabla \cdot \boldsymbol{T}_\mathrm{s}(\boldsymbol{x}, t) + \rho_\mathrm{s}\alpha_\mathrm{s}(\boldsymbol{x}, t)\boldsymbol{g} + \boldsymbol{f}(\boldsymbol{x}, t) \tag{16}$$

Differently from Zitti et al. (2016), here we will not neglect the stress tensor, since the solid phase is not always loosely packed. Furthermore, the interaction force is composed of two contributions: the pressure force and the drag force on the solid phase, i.e.

$$\boldsymbol{f}(\boldsymbol{x}, t) = -\rho_\mathrm{f}\sigma(\boldsymbol{x}, t)\alpha_\mathrm{s}(\boldsymbol{x}, t)\boldsymbol{g} + \sigma(\boldsymbol{x}, t)\delta(\boldsymbol{x}, t)\alpha_\mathrm{s}(\boldsymbol{x}, t)(\boldsymbol{u}_\mathrm{f}(\boldsymbol{x}, t) - \boldsymbol{u}_\mathrm{s}(\boldsymbol{x}, t)) \tag{17}$$

where $\sigma(\boldsymbol{x}, t)$ is the fraction of the solid phase interacting with the fluid phase (i.e. submerged) and $\delta(\boldsymbol{x}, t)$ is a positive function, representing the drag distribution, defined as:

$$\delta(\boldsymbol{x}, t) = \frac{3}{4}c_\mathrm{D}(\boldsymbol{x}, t)\frac{\rho_\mathrm{s}}{d_\mathrm{s}}|\boldsymbol{u}_\mathrm{f}(\boldsymbol{x}, t) - \boldsymbol{u}_\mathrm{s}(\boldsymbol{x}, t)|f_\mathrm{v}(\boldsymbol{x}, t) \tag{18}$$

where $c_{\mathrm{D}}(\boldsymbol{x},t)$ is the drag coefficient, d_{s} is the grain diameter and $f_{\mathrm{v}}(\boldsymbol{x},t)$ is the voidage function (Di Felice 1994). Function (18) provides the amount of drag force associated with the fraction $\sigma(\boldsymbol{x},t)$ of the solid volume $\alpha_{\mathrm{s}}(\boldsymbol{x},t)$ interacting with the fluid, related to the velocity gradient $|\boldsymbol{u}_{\mathrm{f}}(\boldsymbol{x},t)-\boldsymbol{u}_{\mathrm{s}}(\boldsymbol{x},t)|$. Equations (14) to (18) provide the theoretical foundations for developing the equation that describes the mean motion of the impacting mass.

We define a control volume representative of the experimental model, i.e. a two-dimensional volume V, illustrated in Fig. 6, that includes the fluid and gas phases, while the solid phase, composed of grains with mean diameter d_{s}, enters across a section $s(t)$ of the edge AB, with average velocity $\boldsymbol{u}_0=u_0\begin{bmatrix}\cos\theta\\ \sin\theta\end{bmatrix}$. The entering mass is characterized by the bulk density $\rho_0=\phi_0\rho_{\mathrm{s}}$, where ϕ_0 is the solid fraction of the granular bulk entering the control volume. Volume Eqs. (14) and (15) are integrated over the control volume V.

Integration of the mass conservation Eq. (14) for the solid phase gives:

$$\frac{\mathrm{d}V_{\mathrm{s}}(t)}{\mathrm{d}t}=\phi_0u_0\cos\theta s(t)b \tag{19}$$

where $V_{\mathrm{s}}(t)$ is the volume of the solid phase and b is the width of the control volume. Integration of the momentum Eq. (15) leads to:

$$\beta_1\rho_s\frac{\mathrm{d}(V_{\mathrm{s}}(t)\bar{\boldsymbol{u}}_{\mathrm{s}}(t))}{\mathrm{d}t}-\rho_{\mathrm{s}}\phi_0u_0\cos\theta\boldsymbol{u}_0s(t)b=\boldsymbol{R}_{\mathrm{s}}(t) \tag{20}$$

where $\bar{\boldsymbol{u}}_{\mathrm{s}}(t)=\frac{1}{V_{\mathrm{s}}(t)}\int\limits_{V_{\mathrm{s}}(t)}\boldsymbol{u}_{\mathrm{s}}(\boldsymbol{x},t)\mathrm{d}V$ is the mean velocity of the solid phase (hereafter the overbar stands for the volume average); the coefficient β_1, taken as constant for simplicity sake, is such that $\overline{\alpha_{\mathrm{s}}(\boldsymbol{x},t)\boldsymbol{u}_{\mathrm{s}}(\boldsymbol{x},t)}=\beta_1\bar{\alpha}_{\mathrm{s}}(\boldsymbol{x},t)\bar{\boldsymbol{u}}_{\mathrm{s}}(\boldsymbol{x},t)$. $\boldsymbol{R}_{\mathrm{s}}(t)$ is the resultant of the external forces on the whole solid phase, obtained integrating Eq. (16).

The resultant of the external forces $\boldsymbol{R}_{\mathrm{s}}(t)$ must be carefully analysed because it is made of three different contributions:

(1) The divergence of the solid stress tensor

$$\boldsymbol{t}_{\mathrm{s}}(t)=\int\limits_V\nabla\cdot(\boldsymbol{T}_{\mathrm{s}}(x,t))\mathrm{d}V \tag{21}$$

which represents the particle–particle interaction force;

(2) The weight of the solid phase

$$\int\limits_V\rho_{\mathrm{s}}\alpha_{\mathrm{s}}(x,t)g\mathrm{d}V=\rho_{\mathrm{s}}V_{\mathrm{s}}(t)g; \tag{22}$$

(3) The particle–water interaction force, composed of the pressure and drag terms (see Eq. 17). The pressure term corresponds to the buoyancy force integrated over the volume

$$-\int\limits_V\rho_{\mathrm{f}}\sigma(\boldsymbol{x},t)\alpha_{\mathrm{s}}(\boldsymbol{x},t)\boldsymbol{g}\mathrm{d}V=-\rho_{\mathrm{f}}\sigma(t)V_{\mathrm{s}}(t)\boldsymbol{g} \tag{23}$$

where $\sigma(t)$ identifies the submerged fraction of the entire solid volume. The drag term becomes

$$\int_V \sigma(\boldsymbol{x},t)\delta(\boldsymbol{x},t)\alpha_{\mathrm{s}}(\boldsymbol{x},t)(\boldsymbol{u}_{\mathrm{f}}(\boldsymbol{x},t)-\boldsymbol{u}_{\mathrm{s}}(\boldsymbol{x},t))\mathrm{d}V=\beta_2\sigma(t)V_{\mathrm{s}}(t)\delta(t)(\bar{\boldsymbol{u}}_{\mathrm{f}}(t)-\bar{\boldsymbol{u}}_{\mathrm{s}}(t)) \tag{24}$$

where $\bar{\boldsymbol{u}}_f(t)$ is the average velocity of the fluid phase; $\delta(t)$ is a volume-averaged drag function, and the coefficient β_2, taken as constant for simplicity sake, is such that $\overline{\sigma(\boldsymbol{x},t)\delta(\boldsymbol{x},t)\alpha_{\mathrm{s}}(\boldsymbol{x},t)(\boldsymbol{u}_{\mathrm{f}}(\boldsymbol{x},t)-\boldsymbol{u}_{\mathrm{s}}(\boldsymbol{x},t))}=\beta_2\sigma(t)\bar{\alpha}_{\mathrm{s}}(\boldsymbol{x},t)\delta(t)(\bar{\boldsymbol{u}}_{\mathrm{f}}(t)-\bar{\boldsymbol{u}}_{\mathrm{s}}(t))$. Note that the functions $\sigma(t)$ and $\delta(t)$ have a physical meaning different from, respectively, $\sigma(\boldsymbol{x},t)$ and $\delta(\boldsymbol{x},t)$. The latter ones represent the local forces of particle–fluid interaction expressed in terms of pressure and drag, while $\sigma(t)$ and $\delta(t)$ are global functions representing, respectively, the fraction of submerged mass and an averaged drag coefficient.

Using Eqs. (21) to (24), we obtain:

$$\boldsymbol{R}_{\mathrm{s}}(t)=\boldsymbol{t}_{\mathrm{s}}(t)+(\rho_{\mathrm{s}}-\rho_{\mathrm{f}}\sigma(t))V_{\mathrm{s}}(t)\boldsymbol{g}+\beta_2\sigma(t)V_{\mathrm{s}}(t)\delta(t)(\bar{\boldsymbol{u}}_{\mathrm{f}}(t)-\bar{\boldsymbol{u}}_{\mathrm{s}}(t)) \tag{25}$$

In this manner the resultant that appears in Eq. (20) is formulated, as much as possible, as function of the variables that already appear in Eq. (20).

The integrated conservation principles (19) and (20) together with expression (25) give a rather complicated form of the equation for the mean motion of the solid mass $\bar{\boldsymbol{u}}_{\mathrm{s}}(t)$:

$$\begin{aligned}&\beta_1\rho_{\mathrm{s}}\frac{\mathrm{d}V_{\mathrm{s}}(t)}{\mathrm{d}t}\bar{\boldsymbol{u}}_{\mathrm{s}}(t)+\beta_1\rho_{\mathrm{s}}V_{\mathrm{s}}(t)\frac{\mathrm{d}\bar{\boldsymbol{u}}_{\mathrm{s}}(t)}{\mathrm{d}t}-\rho_{\mathrm{s}}\frac{\mathrm{d}V_{\mathrm{s}}(t)}{\mathrm{d}t}\boldsymbol{u}_0\\&=\boldsymbol{t}_{\mathrm{s}}(t)+(\rho_{\mathrm{s}}-\rho_{\mathrm{f}}\sigma(t))V_{\mathrm{s}}(t)\boldsymbol{g}+\beta_2\sigma(t)V_{\mathrm{s}}(t)\delta(t)(\bar{\boldsymbol{u}}_{\mathrm{f}}(t)-\bar{\boldsymbol{u}}_{\mathrm{s}}(t))\end{aligned} \tag{26}$$

In order to simplify it, we exploit the fact that the first and third terms on the right-hand side are both dissipative terms; hence, we collect them and assume that the resultant is in opposition to the solid average velocity:

$$\boldsymbol{t}_{\mathrm{s}}(t)+\beta_2\sigma(t)V_{\mathrm{s}}(t)\delta(t)(\bar{\boldsymbol{u}}_{\mathrm{f}}(t)-\bar{\boldsymbol{u}}_{\mathrm{s}}(t))=-\boldsymbol{D}(t)\bar{\boldsymbol{u}}_{\mathrm{s}}(t) \tag{27}$$

$\boldsymbol{D}(t)$ being a diagonal positive tensor. Substituting Eq. (27) into Eq. (26), after some algebra we get:

$$\begin{aligned}&\beta_1\rho_{\mathrm{s}}V_{\mathrm{s}}(t)\frac{\mathrm{d}\bar{\boldsymbol{u}}_{\mathrm{s}}(t)}{\mathrm{d}t}+\left[\beta_1\rho_{\mathrm{s}}\frac{\mathrm{d}V_{\mathrm{s}}(t)}{\mathrm{d}t}\boldsymbol{I}+\boldsymbol{D}(t)\right]\bar{\boldsymbol{u}}_{\mathrm{s}}(t)\\&=\rho_{\mathrm{s}}\frac{\mathrm{d}V_{\mathrm{s}}(t)}{\mathrm{d}t}\boldsymbol{u}_0+(\rho_{\mathrm{s}}-\rho_{\mathrm{f}}\sigma(t))V_{\mathrm{s}}(t)\boldsymbol{g}\end{aligned} \tag{28}$$

This is a differential equation for the mean motion of the solid phase $\bar{\boldsymbol{u}}_{\mathrm{s}}(t)$. We recognize an inertial term, involving the average acceleration (first term on the left-hand side), a dissipative term, involving the average velocity (second term on the left-hand side) and a non-homogeneous contribution on the right-hand side. The dissipative term is reduced to a unique term defining the dissipative function $\boldsymbol{\varphi}(t)$:

$$\boldsymbol{\varphi}(t)=\beta_1\rho_{\mathrm{s}}\frac{\mathrm{d}V_{\mathrm{s}}(t)}{\mathrm{d}t}\boldsymbol{I}+\boldsymbol{D}(t) \tag{29}$$

Thus, we achieve the simple form:

$$\beta_1 \rho_s V_s(t) \frac{d\bar{\boldsymbol{u}}_s(t)}{dt} + \boldsymbol{\varphi}(t)\bar{\boldsymbol{u}}_s(t) = \rho_s \frac{dV_s(t)}{dt}\boldsymbol{u}_0 + (\rho_s - \rho_f \sigma(t))V_s(t)\boldsymbol{g} \tag{30}$$

Its dimensionless form can be obtained by dividing it by $\rho_s V_s(t) g$, after substituting the terms involving $V_s(t)$ using Eq. (19) and its solution:

$$\beta_1 \frac{d\bar{\boldsymbol{u}}_s^*(t^*)}{dt^*} + \boldsymbol{\varphi}^*(t^*)\bar{\boldsymbol{u}}_s^*(t^*) = \frac{s^*(t^*)}{\int_0^{t^*} s^*(\tau)d\tau}\boldsymbol{u}_0^* + \left(1 - \frac{\rho_f}{\rho_s}\sigma(t^*)\right)\boldsymbol{n_y} \tag{31}$$

where $t^* = t\sqrt{g/h}$ is the dimensionless time, $s^*(t^*) = s(t)/h$ is the dimensionless avalanche thickness, $\bar{\boldsymbol{u}}_s^*(t^*) = \bar{\boldsymbol{u}}_s(t)/\sqrt{gh}$ and $\boldsymbol{u}_0^* = \boldsymbol{u}_0/\sqrt{gh}$ are dimensionless velocities, $\boldsymbol{\varphi}^*(t^*) = \boldsymbol{\varphi}(t)/\rho_s V_s(t)\sqrt{g/h}$ is the dimensionless dissipative function, and $\boldsymbol{n_y} = \begin{bmatrix} 0 \\ 1 \end{bmatrix}$ is the direction of the gravitational field. Equation (31) has now the form of the law of motion of a single body with varying coefficients. In fact, the mean velocity $\bar{\boldsymbol{u}}_s^*(t^*)$ multiplies the dissipative function $\boldsymbol{\varphi}^*(t)$, the non-homogeneous term (right-hand side) is function of both the relative avalanche thickness $s^*(t^*)$ and the dimensionless fraction of submerged mass $\sigma(t^*)$.

Solvability of Eq. (31) depends on the proper definition of the time-dependent functions, which is verified in the following. The physical meaning of the relative avalanche thickness $s^*(t^*)$ and of the dimensionless fraction of submerged mass $\sigma(t^*)$ ensure they are positive definite functions, while the dissipative function $\boldsymbol{\varphi}^*(t)$ requires more attention, since it includes several components. The explicit form of $\boldsymbol{\varphi}^*(t)$ is:

$$\boldsymbol{\varphi}^*(t) = \beta_1 \frac{s^*(t^*)}{\int_0^{t^*} s^*(\tau)d\tau}\boldsymbol{I} + \frac{1}{\rho_s \phi_0 u_0 \cos\theta \int_0^t s(\tau)d\tau b}\boldsymbol{D}(t) \tag{32}$$

$\boldsymbol{\varphi}^*(t)$ is well defined, being $\boldsymbol{I}$ and $\boldsymbol{D}(t)$ diagonal positive tensors, if the denominator of its components is not zero. Since they include $\int_0^{t^*} s^*(\tau)d\tau$, the divergence of the function to infinity occurs when the solid phase is not in the control volume yet. Such condition is easily avoided by assuming the initial time ($t = 0$) to correspond with the impact of the first particle on the water surface, as assumed in Sect. 3, thus ensuring the convergence of Eq. (31) almost everywhere.

Appendix 2: Graphical approach for the analysis of the vertical mean motion of the impacting mass

The analysis of the vertical mean motion of the solid phase is based on use of the $(\sigma(t^*), \psi(t^*))$-plane (see Sect. 3), whose reading is here explained in detail. In the $(\sigma(t^*), \psi(t^*))$-plane the motion is represented in terms of both the submerged fraction of the solid phase and dissipation. By the definition of $\sigma(t^*)$, the representation of the motion of a floating mass is bounded vertically between 0 and 1 (shaded area in Fig. 8a). Further, being $\varphi_y^*(t^*)$ positive, $\psi(t^*)$ has the same sign of the vertical velocity $\bar{u}_{sy}^*(t^*)$. Therefore, the right-hand side of the plane corresponds to positive (downward) velocities, the left-hand side corresponds to negative (upward) velocities, and the condition of zero velocity coincides with the vertical line $\psi(t^*) = 0$. The condition of zero acceleration is given by the line $\sigma(t^*) = \frac{\rho_s}{\rho_f}(1 - \psi(t^*))$, which divides the plane into two parts: the upper part of positive (downward) acceleration and the lower part of negative (upward) acceleration. In the specific case of snow avalanches, the ratio is $\frac{\rho_s}{\rho_f} \sim 0.9$ and the sector of the plane with upward acceleration and upward velocity is small.

The description in the $(\sigma(t^*), \psi(t^*))$-plane of the mean vertical motion of the avalanche is subdivided into several steps:

(1) At impact ($t^* = 0$), the fraction of the submerged mass in the control volume V is zero ($\sigma(0) = 0$) and $\varphi_y^*(t^*)$ does not converge yet (see Appendix 1); hence, the representation of the initial stages of motion is close to the asymptotic condition. Since the initial velocity is downward (i.e. positive), $\psi(0)$ is positive, and the asymptotic condition that represents the initial condition of the motion is $\psi(0) \to +\infty$.

(2) Such initial state of motion, named O in Fig. 8, is located in a region of the plane where the velocity is downward, this increasing the value of $\sigma(t^*)$, and where the acceleration is upward, this reducing the downward velocity itself and, subsequently, $\psi(t^*)$. Hence, the trajectory moves left-upward in the plane (curve OA in Fig. 8a).

(3) In the specific case of snow avalanches the condition of zero velocity is reached before the condition of zero acceleration (point A in Fig. 8a), as proven by experiments. In fact, this condition represents a maximum for the mean vertical position, which occurs in all experiments reported in the bottom panel of Fig. 3. In some cases, the mass could be totally submerged for a while and point A becomes a segment lying on the upper bound.

(4) Since point A is in a region of upward acceleration, the velocity changes its sign and the motion becomes upwards, this gradually reducing the fraction of the submerged mass. Then, the trajectory moves left-downward in the plane, until it reaches zero acceleration (point B in Fig. 8a).

(5) Being B in a region of the plane where the velocity is upward, $\sigma(t^*)$ decreases and the point on the trajectory is pushed down in a region where the acceleration is downward. Thus, the value of the upward velocity decreases and the point representing the motion moves towards the condition of zero velocity (point C).

(6) Point C is placed in a region of downward acceleration, then the downward velocity increases, together with $\sigma(t^*)$, until the trajectory reaches the condition of zero acceleration (Point D).

(7) Point D is characterized by downward velocity, then the trajectory continues upwards in a region where the acceleration is upwards, this decreasing the downward velocity until it vanishes, like in point A. Then, the motion is periodical with smaller amplitudes characterizing each loop, i.e. it is a damped motion.

(8) The oscillations approach the quiescent condition, represented in Fig. 8a through point S, which satisfies both conditions of zero velocity and zero acceleration. For the density ratio typical of the case at hand, the distance between B and S is small and we assume that only one oscillation is needed to attain the quiescent condition.

The representation in the $(\sigma(t^*), \psi(t^*))$-plane supports the qualitative description of the dimensionless mean depth in time $y_C^*(t^*)$: the depth function derived from the representation in Fig. 8a is reported in Fig. 8b. In fact, the position of each point representing the motion illustrates if the depth is increasing or decreasing (downward or upward velocity regions) and if the function is convex or concave (downward or upward acceleration regions). In particular, the points with zero velocity (A and C) correspond to maximum and minimum depths, respectively, and the points with zero acceleration (B and D) are inflection points for the function. In more details: lines OA and DS of Fig. 8a are in a region of upward velocity, that implies an increasing function in Fig. 8b, while ABC is decreasing in Fig. 8b because in Fig. 8a the curve ABC is placed in a region of downward velocity. Further, curve OAB of Fig. 8a is in a region of upward acceleration, this implying the related function of motion to be concave in Fig. 8b and A to be a maximum. Instead, line BCD is in a region of downward acceleration, then the correspondent function is convex in Fig. 8b and B is a local minimum. Since only one oscillation is assumed to occur, the remaining concave curve CS leads to the quiescent condition of zero motion (constant depth in Fig. 8b). In conclusion, the information given by the representation of the motion in the $(\sigma(t^*), \psi(t^*))$-plane has produced a function for the mean depth of the solid phase that has the typical behaviour of a solution of a damped harmonic oscillator.

References

Cremonesi M, Frangi A, Perego U (2010) A lagrangian finite element approach for the simulation of water-waves induced by landslides. Comput Struct 89:1086–1093. doi:10.1016/j.compstruc.2010.12.005

Di Felice R (1994) The voidage function for fluid-particle interaction systems. Int J Multiph Flow 20(1): 153–159. doi:10.1016/0301-9322(94)90011-6

Di Risio M, De Girolamo P, Bellotti G, Panizzo A, Aristodemo F, Molfetta MG, Petrillo AF (2009) Landslide-generated tsunamis runup at the coast of a conical island: new physical model experiments. J Geophys Res Atmos 114:C01009. doi:10.1029/2008jc004858

Frauenfelder R, Jónsson A, Lied K, Shwerdtfeger D, Bergum G, Bühler Y, Stoffel L (2014) Analysis of an artificially triggered avalanche at the Nepheline Syenite Mine on Stjernøya, Alta, Northern Norway. International Snow Science workshop ISSW 2014, At Banff, AB, Canada, pp 689–696. doi: 10.13140/2.1.4471.6807

Fritz HM (2002) Initial phase of landslide generated impulse waves. PhD Thesis Swiss Federal Institute of Technology, Zürich, Switzerland

Fritz HM, Hager WH (2004) Near field characteristics of landslide generated impulse waves. Journal of Waterway Port Coastal and Ocean Engineering 130(6):287–302. doi:10.1061/(ASCE)0733-950X(2004)130:6(287)

Fritz HM, Hager WH, Minor HE (2003a) Landslide generated impulse waves. 1. Instantaneous flow fields. Exp Fluids 35(6):505–519. doi:10.1007/s00348-003-0659-0

Fritz HM, Hager WH, Minor HE (2003b) Landslide generated impulse waves. 2. Hydrodynamic impact crater. Exp Fluids 35(6):520–532. doi:10.1007/s00348-003-0660-7

Fuchs H, Hager WH (2015) Impulse wave modelling and corresponding underwater landslide deposition. In 36th IAHR World Congress, The Hague, the Netherlands (E-proceeding)

Fuchs H, Boes M, Pfister M (2011) Impulse waves at Kühtai reservoir generated by avalanches and landslides. In: International symposium on dams and reservoirs under changing challenges, CRC Press, Taylor & Francis Group, pp 701–708. doi:10.1201/b11669-88

Grilli ST, Watts P (2005) Tsunami generation by submarine mass failure I: Modelling, experimental validation, and sensitivity analyses. J Waterw Port Coast Ocean Eng 131(6):283–297. doi:10.1061/(ASCE)0733-950X(2005)131:6(283)

Harbitz CB, Pedersen G, Gjevik B (1993) Numerical simulations of large water waves due to landslides. J Hydraul Eng 119(12):1325–1342. doi:10.1061/(ASCE)0733-9429(1993)119:12(1325)

Heller V, Hager WH (2010) Impulse product parameter in landslide generated impulse waves. J Waterw Port Coast Ocean Eng 136(3):145–155. doi:10.1061/(ASCE)WW.1943-5460.0000037

Heller V, Hager WH (2014) A universal parameter to predict subaerial landslide tsunamis? J Mar Sci Eng 2:400–412. doi:10.3390/jmse2020400

Heller V, Spinneken J (2015) On the effect of the water body geometry on landslide–tsunamis: physical insight from laboratory tests and 2D to 3D wave parameter transformation. Coast Eng 104:113–134. doi:10.1016/j.coastaleng.2015.06.006

Heller V, Hager WH, Minor HE (2008) Scale effects in subaerial landslide generated impulse waves. Exp Fluids 44(5):691–703. doi:10.1007/s00348-007-0427-7

Huber A, Hager WH (1997) Forecasting impulse waves in reservoirs. 19ème Congrès des Grands Barrages ICOLD, Paris, Florence C31, pp 993–1005

Kamphuis JW, Bowering RJ (1970) Impulse waves generated by landslides. In: 12th conference on coastal engineering, ASCE, NewYork, Washington, vol 1 pp 575–586. doi:10.9753/icce.v12.%25p

Lüthi MP, Vieli A (2016) Multi-method observation and analysis of a tsunami caused by glacier calving. Cryosphere 10:995–1002. doi:10.5194/tc-10-995-2016

Lynett P, Liu PLF (2005) A numerical study of the run-up generated by three-dimensional landslides. J Geophys Res Oceans 110:C03006. doi:10.1029/2004JC002443

Meruane C, Tamburrino A, Roche O (2010) On the role of the ambient fluid on gravitational granular flow dynamics. J Fluid Mech 648:381–404. doi:10.1017/S0022112009993181

Monaghan JJ, Kos A, Issa N (2003) Fluid motion generated by impact. J Waterw Port Coast Ocean Eng 129(6):250–259. doi:10.1061/(ASCE)0733-950X(2003)129:6(250)

Montagna F, Bellotti G, Di Risio M (2011) 3D numerical modeling of landslide-generated tsunamis around a conical island. Nat Hazards 58(1):591–608. doi:10.1007/s11069-010-9689-0

Naaim M (2013) Impulse water waves generated by snow avalanches. Int Snow Sci Workshop Grenoble 2013:619–624

Noda E (1970) Water waves generated by landslides. J Waterw Harbors Coast Eng Div 96(4):835–855

Pelinovsky E, Poplavsky A (1996) Simplified model of tsunami generation by submarine landslides. Phys Chem Earth 21(1–2):13–17. doi:10.1016/S0079-1946(97)00003-7

Pudasaini SP, Miller SA (2012) A real two-phase submarine debris flow and tsunami. In: International conference of numerical analysis and applied mathematics. AIP conference Proceedings 1479(1):197–200. doi:10.1063/1.4756096

Romano A, Di Risio M, Bellotti G, Molfetta MG, Damiani L, De Girolamo P (2016) Tsunamis generated by landslides at the coast of conical islands: experimental benchmark dataset for mathematical model validation. Landslides 13(6):1379–1393. doi:10.1007/s10346-016-0696-4

Slingerland RL, Voight B (1979) Occurrences, properties and predictive models of landslide-generated water waves. In: Voight B (ed) Rockslides and Avalanches 2—engineering sites. Elsevier, Amsterdam, pp 317–397

Truesdell C (1984) Rational thermodynamics. Springer Science & Business Media, New York

Vacondio R, Mignosa P, Pagani S (2013) 3D SPH numerical simulation of the wave generated by the Vajont Rockslide. Adv Water Resour 59:146–156. doi:10.1016/j.advwatres.2013.06.009

Zitti G (2016) Avalanche-induced impact water waves. PhD Thesis, Università Politecnica delle Marche, Ancona, Italy

Zitti G, Ancey C, Postacchini M, Brocchini M (2016) Impulse waves generated by snow avalanches: momentum and energy transfer to a water body. J Geophys Res Earth Surf 121(12):2399–2423. doi:10.1002/2016JF003891

Zweifel A, Hager WH, Minor HE (2006) Plane impulse waves in reservoirs. J Waterw Port Coast Ocean Eng 132(5):358–368. doi:10.1061/(ASCE)0733-950X(2006)132:5(358)